

EFFICIENT IMPLEMENTATION OF HIGHER-ORDER FINITE VOLUME TIME-DOMAIN METHOD FOR ELECTRICALLY LARGE SCATTERERS

A. Chatterjee[†] and R.-S. Myong

Research Center for Aircraft Parts Technology
Gyeongsang National University
Jinju, Kyeongnam 660–701, South Korea

Abstract—The Finite Volume Time-Domain (FVTD) method finds limited application in the simulation of electromagnetic scattering from electrically large scatterers because of the fine discretization required in terms of points-per-wavelength. An efficient implementation of a higher-order FVTD method is proposed for electrically large, perfectly conducting scatterers. Higher-order and fine-grid accuracy are preserved, despite using only a first-order spatial accuracy and a coarse grid in substantial parts of the FVTD computational domain, by partially incorporating a time-domain Physical Optics (PO) approximation for the surface current. This can result in considerable savings in computational time while analyzing geometries containing electrically large, smooth sections using the FVTD method. The higher-order FVTD method in the present work is based on an Essentially Non-Oscillatory (ENO) reconstruction and results are presented for two-dimensional perfectly conducting scatterers subject to Transverse Magnetic (TM) or Transverse Electric (TE) illumination.

1. INTRODUCTION

Higher-order, characteristic based numerical schemes are usually used to solve the time-domain Maxwell's equations written as a system of hyperbolic conservation laws in the Finite Volume Time-Domain (FVTD) method [1–3]. Electromagnetic scattering involving complex geometries, broad-band signals and diverse material properties can be dealt with advantageously using the FVTD method [3–6]. In

Corresponding author: A. Chatterjee (avijit@aero.iitb.ac.in).

[†] Also with Department of Aerospace Engineering, Indian Institute of Technology, Bombay, Mumbai 400076, India.

spite of these advantages, the FVTD method is rarely used for engineering applications like predicting the Radar Cross Section (RCS) of realistic geometries at frequency bands of practical interest. The major drawback of the FVTD method is the requirement of large computational time for simulations involving high frequencies. Rigorous numerical techniques for solving the Maxwell's equations, including the popular Finite Difference Time Domain (FDTD) method [4], share this common disadvantage when dealing with electrically large scatterers.

The large computational time at higher frequencies is mainly related to the fine grid required by FVTD and FDTD methods to contain numerical dispersion errors. The computational grid for FVTD and FDTD methods can be based on resolutions of 15–20 Points-Per-Wavelength (PPW) [4], making simulations involving electrically large scatterers prohibitively expensive. Higher-order numerical schemes which result in lower dispersion error are traditionally used by FVTD and FDTD methods to reduce the number of grid points in the computational domain while maintaining required levels of accuracy [7, 8]. Solution adaptive grids with variable grid density can similarly be used to increase computational efficiency, especially for numerical simulation involving multiple scales, by using optimal number of grid points. Subgridding is employed in time-domain simulation of the Maxwell equations to account for subgrid scale effects in the computational domain [9] using locally refined meshes.

In the present work, an efficient implementation of a higher-order FVTD method is proposed for simulation of electromagnetic scattering from electrically large, perfectly conducting scatterers. The spatial accuracy of the numerical scheme as well as the computational mesh used in the proposed FVTD implementation are not uniform. The computational domain is split into multiple regions. Each region either employs a first-order accurate spatial discretization and a coarse grid or a higher-order spatial discretization and a fine grid. The overall accuracy of the solution obtained is shown to be similar to that of a higher-order accurate FVTD scheme on an uniform fine grid. Overall higher-order and fine-grid accuracy are preserved, despite using only a first-order accurate numerical scheme and a coarse grid in substantial parts of the FVTD computational domain, by partially expressing the surface current density for the scatterer using an asymptotic Physical Optics (PO) approximation.

In literature, hybrid methods have been proposed based on the combination of rigorous techniques like Method of Moments (MOM) and FDTD with ray or current based high-frequency asymptotic approaches for increased computational efficiency while dealing with

electrically large scatterers [10–13]. Increased computational efficiency for the FVTD method has also been addressed through use of local time-stepping [14] and hybrid FVTD-integral Equation (15) approaches. In the proposed implementation, the surface current for a perfectly conducting scatterer is expressed locally using either only the incident field (as in a PO approximation) or as a combination of the incident field and a higher-order FVTD computed scattered field. The proposed FVTD implementation can also be viewed as a current based hybrid method in the time-domain combining FVTD and PO techniques. Previous attempts in literature at combining FDTD and time-domain PO methods assume the existence of multiple scatterers of different electrical sizes which are treated appropriately by either FDTD or PO methods [12, 13]. High-frequency PO approximations for equivalent surface currents are normally valid for electrically large, smooth sections of a scatterer. Thus, the proposed FVTD implementation is directed towards geometries with smooth, electrically large sections like nose radomes [11] and reflector antennas [16]. Preliminary related work, reported in [17], mainly considered FVTD computations on an uniform coarse grid for electrically large scatterers along with a PO approximation for resolving dominant specular returns. The proposed implementation is described in the present work for two-dimensional perfectly conducting geometries subject to Transverse Magnetic (TM) or Transverse Electric (TE) illumination. The present work uses an Essentially Non-Oscillatory (ENO) [18, 19] based spatial discretization with which arbitrary higher-order accuracy can be achieved. Maintaining an overall higher-order and fine-grid accuracy, despite using only a first-order accurate numerical scheme and a coarse grid in substantial parts of the computational domain, can significantly speed up FVTD computations for geometries containing electrically large smooth regions.

2. GOVERNING EQUATIONS

The three-dimensional Maxwell's curl equations, in the differential form in free space, can be expressed as

$$\frac{\partial \mathbf{B}}{\partial t} = -\nabla \times \mathbf{E} \quad (1)$$

$$\frac{\partial \mathbf{D}}{\partial t} = \nabla \times \mathbf{H} - \mathbf{J}_i \quad (2)$$

where \mathbf{B} is the magnetic induction, \mathbf{E} the electric field vector, \mathbf{D} the electric field displacement and \mathbf{H} the magnetic field vector. \mathbf{J}_i is the

impressed current density vector, $\mathbf{D} = \varepsilon\mathbf{E}$, $\mathbf{B} = \mu\mathbf{H}$ with ε and μ respectively the permittivity and permeability in free space.

The time-domain Maxwell's equations can also be written in a conservative total field form as

$$\frac{\partial \mathbf{u}}{\partial t} + \frac{\partial \mathbf{f}(\mathbf{u})}{\partial x} + \frac{\partial \mathbf{g}(\mathbf{u})}{\partial y} + \frac{\partial \mathbf{h}(\mathbf{u})}{\partial z} = \mathbf{s} \quad (3)$$

where

$$\mathbf{u} = \begin{pmatrix} B_x \\ B_y \\ B_z \\ D_x \\ D_y \\ D_z \end{pmatrix}, \quad \mathbf{f} = \begin{pmatrix} 0 \\ -D_z/\varepsilon \\ D_y/\varepsilon \\ 0 \\ B_z/\mu \\ -B_y/\mu \end{pmatrix}, \quad \mathbf{g} = \begin{pmatrix} D_z/\varepsilon \\ 0 \\ -D_x/\varepsilon \\ -B_z/\mu \\ 0 \\ B_x/\mu \end{pmatrix},$$

$$\mathbf{h} = \begin{pmatrix} -D_y/\varepsilon \\ D_x/\varepsilon \\ 0 \\ B_y/\mu \\ -B_x/\mu \\ 0 \end{pmatrix}, \quad \mathbf{s} = \begin{pmatrix} 0 \\ 0 \\ 0 \\ -J_{ix} \\ -J_{iy} \\ -J_{iz} \end{pmatrix} \quad (4)$$

subscripts indicate scalar components in the Cartesian x , y , z directions. In two dimensions, Maxwell's equations can be split into two sets of systems. These are the equations for TM and TE waves. The two-dimensional conservative form is written as

$$\frac{\partial \mathbf{u}}{\partial t} + \frac{\partial \mathbf{f}(\mathbf{u})}{\partial x} + \frac{\partial \mathbf{g}(\mathbf{u})}{\partial y} = \mathbf{s} \quad (5)$$

The vectors in Equation (5) for the TM waves are

$$\mathbf{u} = \begin{pmatrix} B_x \\ B_y \\ D_z \end{pmatrix}, \quad \mathbf{f} = \begin{pmatrix} 0 \\ -D_z/\varepsilon \\ -B_y/\mu \end{pmatrix}, \quad \mathbf{g} = \begin{pmatrix} D_z/\varepsilon \\ 0 \\ B_x/\mu \end{pmatrix}, \quad \mathbf{s} = \begin{pmatrix} 0 \\ 0 \\ -J_{iz} \end{pmatrix} \quad (6)$$

while that for the TE waves are

$$\mathbf{u} = \begin{pmatrix} B_z \\ D_x \\ D_y \end{pmatrix}, \quad \mathbf{f} = \begin{pmatrix} D_y/\varepsilon \\ 0 \\ B_z/\mu \end{pmatrix}, \quad \mathbf{g} = \begin{pmatrix} -D_x/\varepsilon \\ -B_z/\mu \\ 0 \end{pmatrix}, \quad \mathbf{s} = \begin{pmatrix} 0 \\ -J_{ix} \\ -J_{iy} \end{pmatrix}. \quad (7)$$

3. NUMERICAL SCHEME

3.1. Finite Volume Time-Domain Method

The FVTD method usually solves the integral form of the conservative Maxwell's equations in a scattered field formulation with the incident

field assumed to be a solution of the Maxwell's equations in free space. Integrating the differential form of the conservation law, represented by Equation (3), in the absence of a source term over an arbitrary control volume Ω ,

$$\frac{\partial \int_{\Omega} \mathbf{u}^s dV}{\partial t} + \int_{\Omega} \nabla \cdot (\mathbf{F}(\mathbf{u}^s)) dV = 0. \tag{8}$$

\mathbf{F} is the flux vector with components \mathbf{f} , \mathbf{g} , \mathbf{h} in the Cartesian x , y , z directions with superscript 's' indicating scattered field variables. Applying the divergence theorem, the integral form of the conservation law is obtained as

$$\frac{\partial \int_{\Omega} \mathbf{u}^s dV}{\partial t} + \oint_S \mathbf{F}(\mathbf{u}^s) \cdot \hat{\mathbf{n}} dS = 0 \tag{9}$$

with $\hat{\mathbf{n}}$ the outward unit normal vector. The above integral form is discretized and solved for in the FVTD method. For three-dimensional problems, the domain can be discretized into hexahedral cells and the integral form applied to individual cells. The corresponding discretization for 2D problems consists of quadrilateral cells. The discretized form for the k th cell in a three-dimensional cell-centered formulation is

$$\Omega_k \frac{d\bar{\mathbf{u}}_k^s}{dt} + \sum_{j=1}^6 \left[(\mathbf{F}(\mathbf{u}^s) \cdot \hat{\mathbf{n}}S)_j \right]_k = 0 \tag{10}$$

where $\bar{\mathbf{u}}_k^s$ indicates the volume average of \mathbf{u}^s over cell k and $[(\mathbf{F}(\mathbf{u}^s) \cdot \hat{\mathbf{n}}S)_j]_k$ the average flux through face j of cell k . The equivalent two-dimensional form solved for in the present work is

$$A_k \frac{d\bar{\mathbf{u}}_k^s}{dt} + \sum_{j=1}^4 \left[(\mathbf{F}(\mathbf{u}^s) \cdot \hat{\mathbf{n}}s)_j \right]_k = 0 \tag{11}$$

where A_k represents the cell area. Equations (10) and (11) represent generic systems of hyperbolic conservation laws discretized in a finite volume framework and can be solved using a variety of numerical schemes [20].

In the present work, the 2D Maxwell's equations in its discretized form in Equation (11), are solved using a higher-order ENO [18, 19] spatial discretization and a second order Runge-Kutta time integration. The ENO scheme, as in previous three-dimensional FVTD applications [5, 6], is in the ENO-Roe form [18, 19], which

efficiently implements the ENO reconstruction based on the numerical fluxes instead of the cell averaged state variables. This for the scalar hyperbolic conservation law

$$u_t + f(u)_x = 0, \quad (12)$$

has the spatial derivative at the i th grid point approximated as

$$\frac{\partial f(u)}{\partial x} \Big|_i = \frac{1}{\Delta x} \left(\bar{f}_{i+1/2} - \bar{f}_{i-1/2} \right) + \mathcal{O}(\Delta x^q) \quad (13)$$

where Δx is the grid size, q the order of the scheme, $\bar{f}_{i+1/2}$ the numerical flux function at the right cell-face. The r th order accurate reconstruction of the numerical flux in the ENO scheme is

$$\bar{f}_{i+1/2} = \sum_{l=0}^{r-1} \alpha_{k,l}^r f_{i-r+1+k+l} \quad (14)$$

where $\alpha_{k,l}^r$ are the reconstruction coefficients and k the stencil index selected among the r candidate stencils. The stencil S_k can be written as

$$S_k = (x_{i+k-r+1}, x_{i+k-r+2}, \dots, x_{i+k}) \quad (15)$$

and is locally the smoothest possible stencil. Details regarding reconstruction coefficients and stencil selection for ENO schemes are widely available in literature including Refs. [18, 19]. Extension to the two-dimensional system of Equation (5) is obtained by decoupling the system into three scalar hyperbolic conservation laws normal to the cell faces [5].

For perfect electric conductors solved for in the present work, the total tangential electric field $\hat{\mathbf{n}} \times \mathbf{E} = \mathbf{0}$ on the conducting surface. Standard characteristic boundary conditions can be implemented at the outer boundary with the scattered field variables being taken as zero in the far field.

3.2. Proposed FVTD Implementation

In the proposed implementation, the current on the surface of an electrically large, perfectly conducting scatterer is expressed locally using either the incident field or an appropriate combination of the incident and higher-order FVTD computed scattered field. The surface current density vector, in the time-domain for a perfect conductor, is defined as

$$\mathbf{J}_{\text{sur}}(\mathbf{r}, t) = \hat{\mathbf{n}} \times \mathbf{H}(\mathbf{r}, t). \quad (16)$$

This can be decomposed into contributions from the incident (i) and scattered (s) fields and written as

$$\mathbf{J}_{\text{sur}}(\mathbf{r}, t) = \hat{\mathbf{n}} \times [\mathbf{H}^i(\mathbf{r}, t) + \mathbf{H}^s(\mathbf{r}, t)]. \quad (17)$$

In the proposed FVTD implementation, the surface of the perfectly conducting scatterer is divided into FVTD, PO and “transition” parts based on the evaluation of the surface current. Surface currents defined for FVTD, PO and transition parts differ based on the local approximation for the scattered magnetic field vector $\mathbf{H}^s(\mathbf{r}, t)$ in Equation (17).

The surface current density for the FVTD part is defined as

$$\mathbf{J}_{\text{sur}}^{\text{FVTD}}(\mathbf{r}, t) = \hat{\mathbf{n}} \times [\mathbf{H}^i(\mathbf{r}, t) + \mathbf{H}^{s'}(\mathbf{r}, t)] \quad (18)$$

where (s') indicates the scattered field computed using a higher-order FVTD method. Approximating the scattered field in Equation (17) using the local incident field leads to the PO approximated surface current

$$\mathbf{J}_{\text{sur}}^{\text{PO}}(\mathbf{r}, t) = \hat{\mathbf{n}} \times [\mathbf{H}^i(\mathbf{r}, t) \pm \mathbf{H}^i(\mathbf{r}, t)], \quad (19)$$

defined for PO parts of the scatterer surface. $\mathbf{J}_{\text{sur}}^{\text{PO}}(\mathbf{r}, t) = 2\hat{\mathbf{n}} \times \mathbf{H}^i$, is commonly used to approximate the surface current density on smooth lit parts of a perfectly conducting scatterer in the PO method, with $\mathbf{J}_{\text{sur}}^{\text{PO}} = 0$ in the shadow region. Both these approximations are combined to form Equation (19) using the \pm operator.

The scattered field, in Equation (17), is replaced by a linear combination of the local incident field and the higher-order FVTD computed scattered field to yield the surface current in the transition part. This requires to be implemented differently for TM and TE waves. For the TE system, described in Equations (5) and (7), the transitional surface current is defined as

$$\mathbf{J}_{\text{sur}}^{\text{trans}}(\mathbf{r}, t) = \hat{\mathbf{n}} \times \left[\mathbf{H}_z^i(\mathbf{r}, t) \pm \left\{ \zeta \mathbf{H}_z^i(\mathbf{r}, t) \pm (1 - \zeta) \mathbf{H}_z^{s'}(\mathbf{r}, t) \right\} \right] \hat{\mathbf{k}} \quad (20)$$

with $\hat{\mathbf{k}}$ the unit vector in the Cartesian z direction. The equivalent transitional surface current for the TM system, described in Equations (5) and (6), is

$$\mathbf{J}_{\text{sur},z}^{\text{trans}}(\mathbf{r}, t) \hat{\mathbf{k}} = \hat{\mathbf{n}} \times \mathbf{H}^i(\mathbf{r}, t) \pm \left[\zeta \left\{ \hat{\mathbf{n}} \times \mathbf{H}^i(\mathbf{r}, t) \right\} \pm (1 - \zeta) \left\{ \hat{\mathbf{n}} \times \mathbf{H}^{s'}(\mathbf{r}, t) \right\} \right]. \quad (21)$$

The transitional surface current connects the FVTD to either a lit or shadow PO region. Using $+(-)$ in the \pm operator in Equations (20) and (21) recovers the transitional current between FVTD and lit

(shadow) PO region. $\zeta = [0, 1]$ and Equations (20) and (21) satisfy $\mathbf{J}_{\text{sur}}^{\text{trans}}(\mathbf{r}(\zeta = 0), t) = \mathbf{J}_{\text{sur}}^{\text{FVTD}}(\mathbf{r}, t)$ and $\mathbf{J}_{\text{sur}}^{\text{trans}}(\mathbf{r}(\zeta = 1), t) = \mathbf{J}_{\text{sur}}^{\text{PO}}(\mathbf{r}, t)$ irrespective of a lit or shadow PO region being referred to.

In the proposed implementation, the surface current density on smooth lit as well as shadow parts of the perfectly conducting scatterer can be appropriately defined using the (lit or shadow) PO approximation $\mathbf{J}_{\text{sur}}^{\text{PO}}$. The FVTD computed current $\mathbf{J}_{\text{sur}}^{\text{FVTD}}$ is considered to be valid at locations on the scatterer surface where a basic PO approximation leads to erroneous scattered fields like shadow boundaries of curved surfaces [21] and edge discontinuities. $\mathbf{J}_{\text{sur}}^{\text{trans}}$ is used to define the surface current density in transition regions connecting FVTD and PO currents. In the proposed implementation, regions in the FVTD computational domain bounded by the scatterer surface with PO approximated surface currents $\mathbf{J}_{\text{sur}}^{\text{PO}}$ are evaluated using a first-order accurate upwind scheme and a coarse grid. A higher-order ENO scheme and a fine grid is used for the rest of the computational domain. A first-order accurate upwind scheme is also obtained by simply invoking the option of a first-order spatial accuracy in the higher-order ENO scheme used for the rest the domain. The basic FVTD implementation can be illustrated using the example of RCS computations involving a two-dimensional, electrically large, perfectly conducting, circular cylinder. The implementation shown in Figure 1, has the PO approximation for the surface current valid on lit and shadow parts of the scatterer, excluding areas close to the shadow boundary. The computational domain is split into multiple regions based on the definition of the surface current. In regions 1 and 1', only a first-order upwind scheme and a coarse grid is used, with the current on the bounding scatterer surface appropriately based on lit or shadow-PO approximations $\mathbf{J}_{\text{sur}}^{\text{PO}}$. In regions 2, 2' and 3, a higher-order ENO scheme and a fine grid is utilized. The higher-order FVTD computed surface current $\mathbf{J}_{\text{sur}}^{\text{FVTD}}$ is used for the scatterer surface bounding region 3. Transitional currents $\mathbf{J}_{\text{sur}}^{\text{trans}}$ are considered to be valid for region 2 and 2', and appropriately connect PO and FVTD parts of the scatterer.

The coarse grid used in the FVTD implementation can be based on an average resolution of 2–4 PPW. This is the resolution usually required on the scatterer surface for a satisfactory numerical evaluation of the PO integral in order to obtain the scattered far-field from PO approximated surface currents [16]. This could also be considered the minimum resolution required in a FVTD (or FDTD) method to satisfactorily predict the scattered far-field in the absence of any discretization error. The fine grid used is based on a regular FVTD resolution of 15–20 PPW [4]. The surface current density is calculated based on the local definition in the time-domain and complex currents

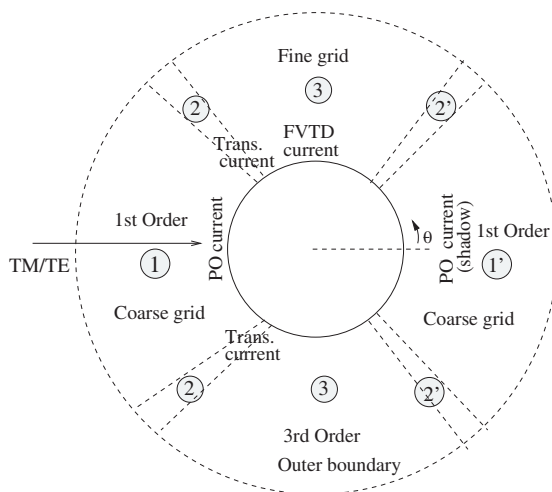


Figure 1. Proposed implementation for circular cylinder.

in the frequency-domain computed from the time history using a Fourier transform. Predicting the RCS requires the scattered field intensity at infinity which is obtained from complex surface currents using a near-to-far field transformation [22].

The proposed FVTD implementation is summarized in the following steps:

1. The scatterer surface is divided into PO (shadow and lit), FVTD and transition parts based on the evaluation of the surface current as $\mathbf{J}_{\text{sur}}^{\text{PO}}$ or $\mathbf{J}_{\text{sur}}^{\text{FVTD}}$ or $\mathbf{J}_{\text{sur}}^{\text{trans}}$.
2. FVTD computations are carried out using a first-order upwind scheme and a coarse mesh for regions in the computational domain bounded by the scatterer surface with a PO approximated value $\mathbf{J}_{\text{sur}}^{\text{PO}}$ (shadow or lit) for the surface current. A higher-order ENO scheme and a fine grid is used elsewhere in the computational domain.
3. The surface current is calculated in the time-domain based on the locally valid current definition.
4. Complex currents, in the frequency domain, on the scatterer surface, computed using the time history. The scattered field intensity at infinity calculated from the complex currents using a near-to-far field transformation.

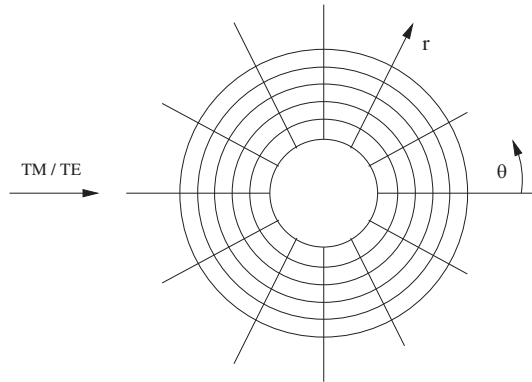


Figure 2. O grid for circular cylinder, schematic.

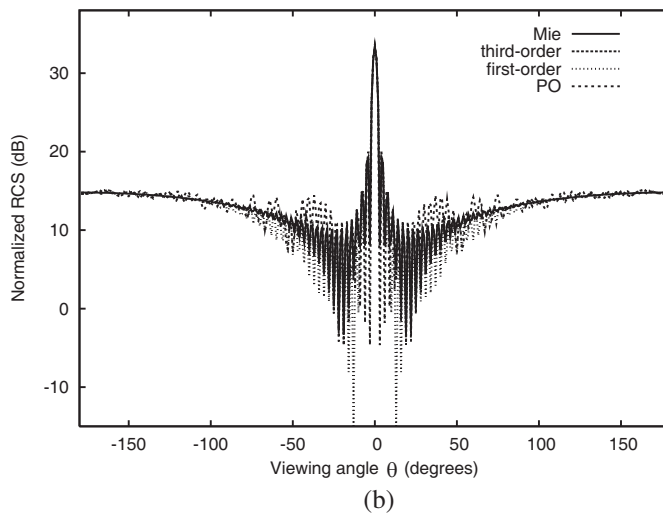
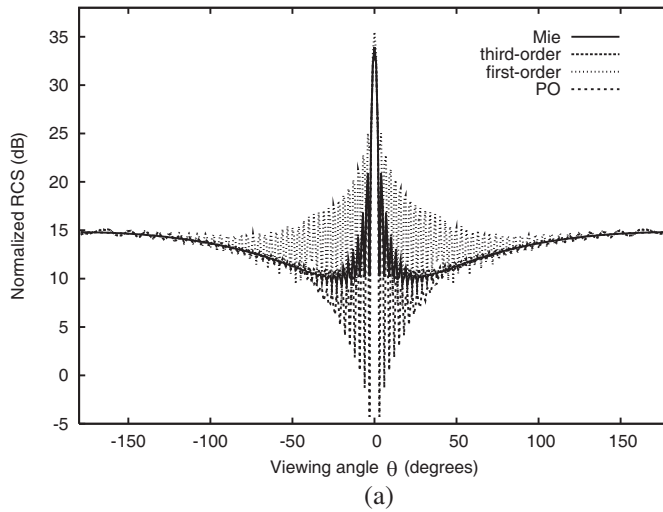
4. NUMERICAL SOLUTIONS — CIRCULAR CYLINDER

The efficacy of this FVTD implementation is initially demonstrated at length by computing for RCS of 2D, electrically large, perfectly conducting, circular cylinders. Results are presented for electrical sizes corresponding to $a/\lambda = 9.6$ and $a/\lambda = 14.4$ where a is the cylinder radius and λ the wavelength of the continuous harmonic incident TE or TM wave. An ‘O’ type boundary fitted grid is used for FVTD computations with the number of points in the radial direction always fixed at 50. The grid is shown in the form of a schematic in Figure 2. The fine grid at $a/\lambda = 9.6$ consists of 800 uniformly spaced grid points in the circumferential direction corresponding to a grid resolution of 13.3 PPW on the scatterer surface. The corresponding fine grid at $a/\lambda = 14.4$ has a surface resolution of 17.7 PPW and 1600 uniformly spaced points in the circumferential direction. The higher-order FVTD method is based on a third-order ENO reconstruction.

4.1. Spatial Order of Accuracy

We initially show the effect of order of spatial accuracy on computed FVTD solutions for above-mentioned 2D, electrically large circular cylinders before discussing results from the proposed FVTD implementation. FVTD results obtained using uniform third-order or first-order spatial accuracy are compared with basic PO and the exact or Mie series solutions. The results presented are in the form of the bistatic RCS (normalized with respect to the wavelength) and are shown in Figs. 3(a)–(d). $\theta = \pm 180^\circ$ indicates the monostatic point in all circular cylinder bistatic plots. Both first and third-

order spatially accurate solutions are obtained on “fine-grids” specified previously for respective values of a/λ . In all the cases considered, the first-order accurate solution (at these grid resolutions) show considerable deviation from the exact solution away from very-near-specular regions. In contrast, the bistatic RCS obtained using a third-order ENO based FVTD method compares well with the exact bistatic solution (see Figs. 3(a)–(d)). In the context of the PO technique, it has been shown that a larger sampling interval can be used for evaluation of near-specular scattering from extremely large, smooth



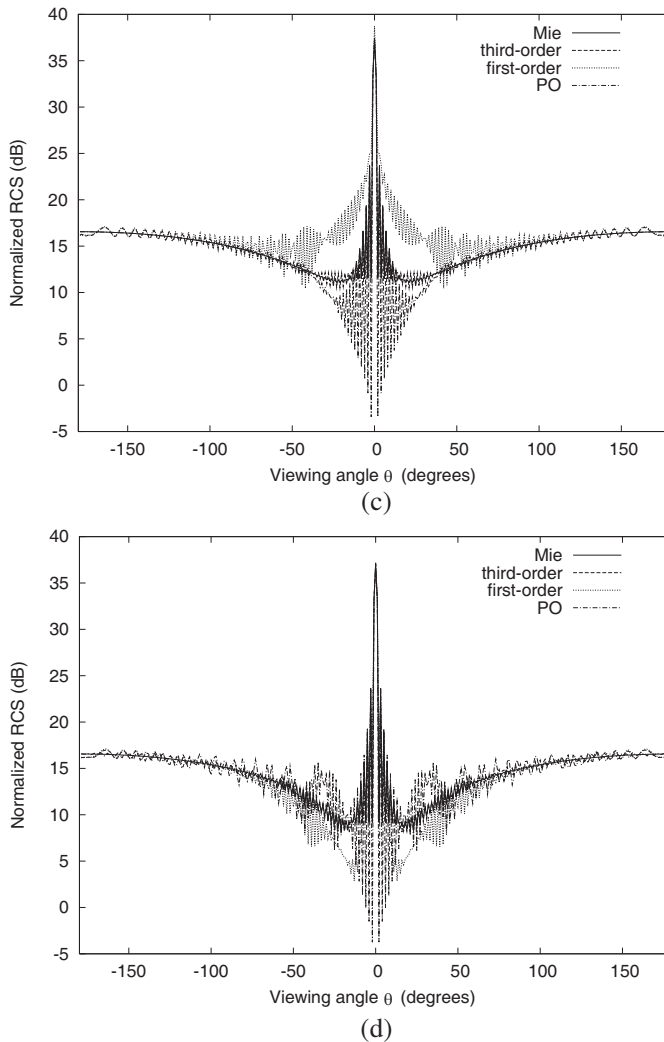


Figure 3. Effect of spatial order of accuracy. (a) $a/\lambda = 9.6$, TM, (b) $a/\lambda = 9.6$, TE, (c) $a/\lambda = 14.4$, TM, (d) $a/\lambda = 14.4$, TE.

structures [16]. This was demonstrated in [16] by computing the radiation pattern of a large reflector antenna. Present results for 2D circular cylinders, in Figs. 3(a)–(d), similarly indicate that only very-near-specular scattering can possibly be predicted for similar geometries using first-order spatially accurate FVTD methods for a reasonable discretization. The accuracy of the first-order accurate

FVTD solution rapidly degrades away from very-near-specular regions. A corresponding behavior is again seen in PO methods when very large, smooth structures are evaluated using an uniformly large sampling interval defined on the basis of near-specular scattering [16]. The effect of discretization on computed FVTD solution is similar to that of spatial order of accuracy, with FVTD methods on coarse meshes being able to resolve only very-near-specular scattering accompanied by rapid deterioration in accuracy away from the specular. Additionally, the inaccuracy of PO solutions away from near-specular regions, due to discontinuous modeling of the surface current at shadow boundaries in the basic PO approximation, is apparent in results for 2D circular cylinders in Figs. 3(a)–(d). The proposed FVTD implementation is based on the use of higher-order, fine-grid FVTD computed surface currents for locations on a electrically large, perfectly conducting scatterer where the basic PO approximation proves inadequate.

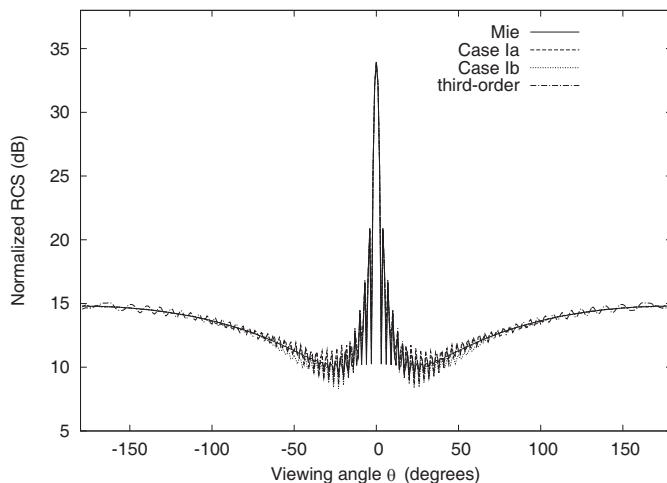
4.2. Efficient FVTD Implementation

We consider an initial FVTD implementation with regions 1 and 1' bounded by scatterer surface with PO approximated surface current, evaluated using first-order accurate spatial accuracy but on the same fine discretization used for regions 2, 2' and 3 where third-order spatial accuracy is utilized (see Figure 1). This initial implementation is referred to as case I. The final FVTD implementation with regions 1 and 1' evaluated using both first-order spatial accuracy and a coarse grid exactly as described in the previous section, is termed case II. Case I (II) is further divided into cases Ia (IIa) and Ib (IIb) based on size of regions 1 and 1' in the FVTD computational domain. Table 1

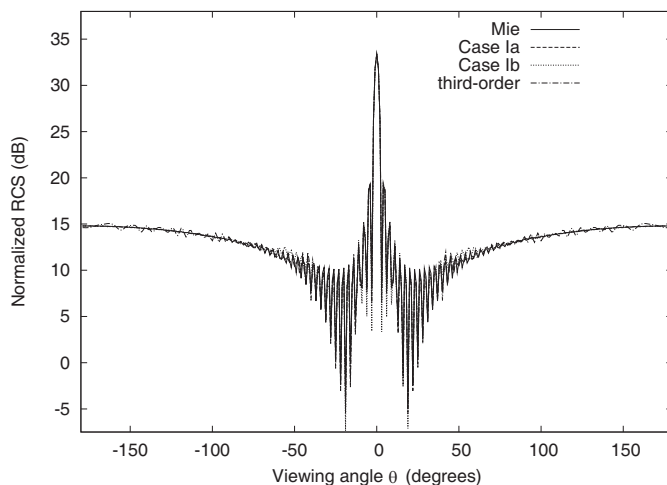
Table 1. FVTD implementation — Cases I and II.

Cases	a/λ	region 1	region 1'	coarse grid (PPW)
Ia	9.6	$[135^\circ, 225^\circ]$	$[45^\circ, -45^\circ]$	14.4 (fine grid)
Ib	9.6	$[112.5^\circ, 247.5^\circ]$	$[67.5^\circ, -67.5^\circ]$	14.4 (fine grid)
Ia	14.4	$[135^\circ, 225^\circ]$	$[45^\circ, -45^\circ]$	17.7 (fine grid)
Ib	14.4	$[112.5^\circ, 247.5^\circ]$	$[67.5^\circ, -67.5^\circ]$	17.7 (fine grid)
IIa	9.6	$[135^\circ, 225^\circ]$	$[45^\circ, -45^\circ]$	3.32
IIb	9.6	$[112.5^\circ, 247.5^\circ]$	$[67.5^\circ, -67.5^\circ]$	4.43
IIa	14.4	$[135^\circ, 225^\circ]$	$[45^\circ, -45^\circ]$	2.12
IIb	14.4	$[112.5^\circ, 247.5^\circ]$	$[67.5^\circ, -67.5^\circ]$	2.95

lists extent of regions 1 and 1' along with resolution of coarse grid in terms of PPW on the surface of the circular cylinder for all the cases considered here (see also Figure 1). The coarse grids in region 1 and 1' for cases IIa and IIb respectively have resolutions of 3.32 (2.12) PPW and 4.43 (2.95) PPW on the scatterer surface for $a/\lambda = 9.6$ (14.4). Definitions for case IIa and IIb are listed in Table 1. Transition regions 2 and 2' measure a few wavelengths on the scatterer surface. Results presented for case I in Figs. 4(a)–(d) compare the computed bistatic RCS with exact and third-order accurate FVTD results. The use of



(a)



(b)

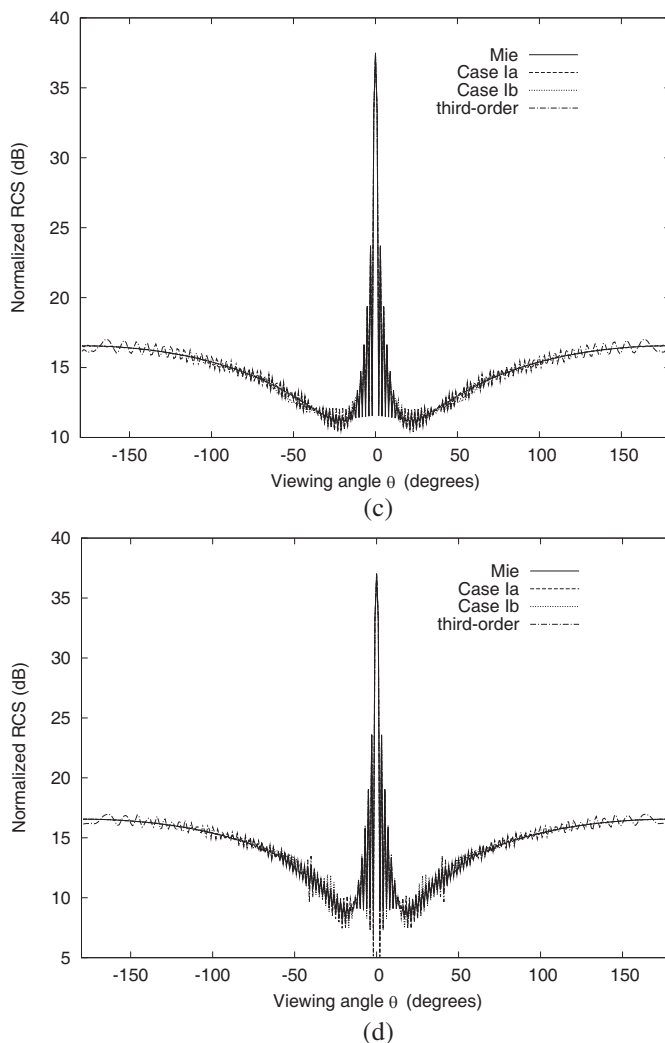
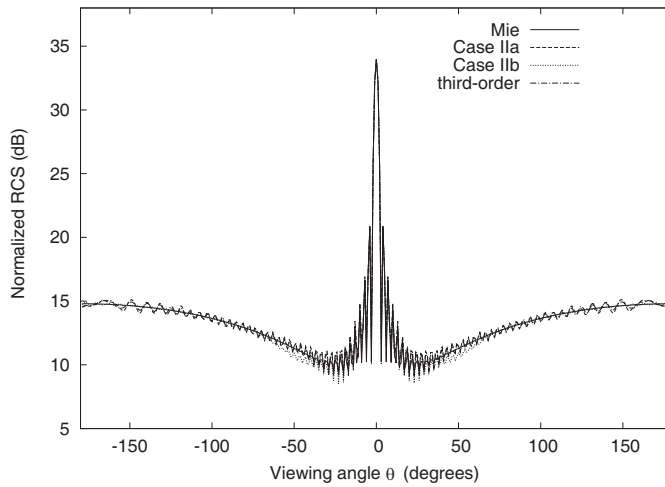


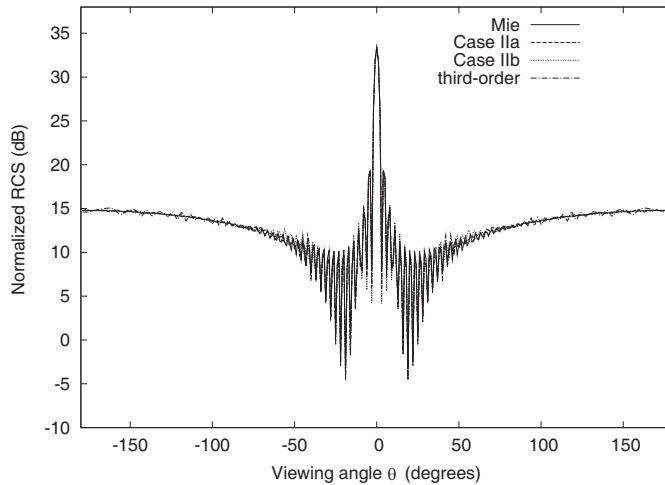
Figure 4. Case I implementation (first-order on fine grid). (a) $a/\lambda = 9.6$, TM, (b) $a/\lambda = 9.6$, TE, (c) $a/\lambda = 14.4$, TM, (d) $a/\lambda = 14.4$, TE.

PO approximated currents on the scatterer surface bounding regions 1 and 1' preserves an overall third-order accuracy in the computed results despite using only a first-order spatial accuracy in a majority of the computational domain. Results in Figs. 5(a)–(d) similarly show that third-order and fine-grid accuracy are maintained, despite using only a first-order accurate spatial accuracy and a coarse grid in regions 1 and 1' of the FVTD computational domain, by partially

expressing the surface current using a PO approximation. Most of the computational cost incurred in the proposed implementation is in the fine-grid and higher-order accurate FVTD computations required for regions 3, 2 and 2' of the computational domain. For the rest of the computational domain, only a first-order spatial accuracy is used, and the average resolution can be a fraction of that in the fine grid. Case II implementation is achieved here at approximately 40% of the computational cost required for the higher-order FVTD technique on an uniform fine grid.



(a)



(b)

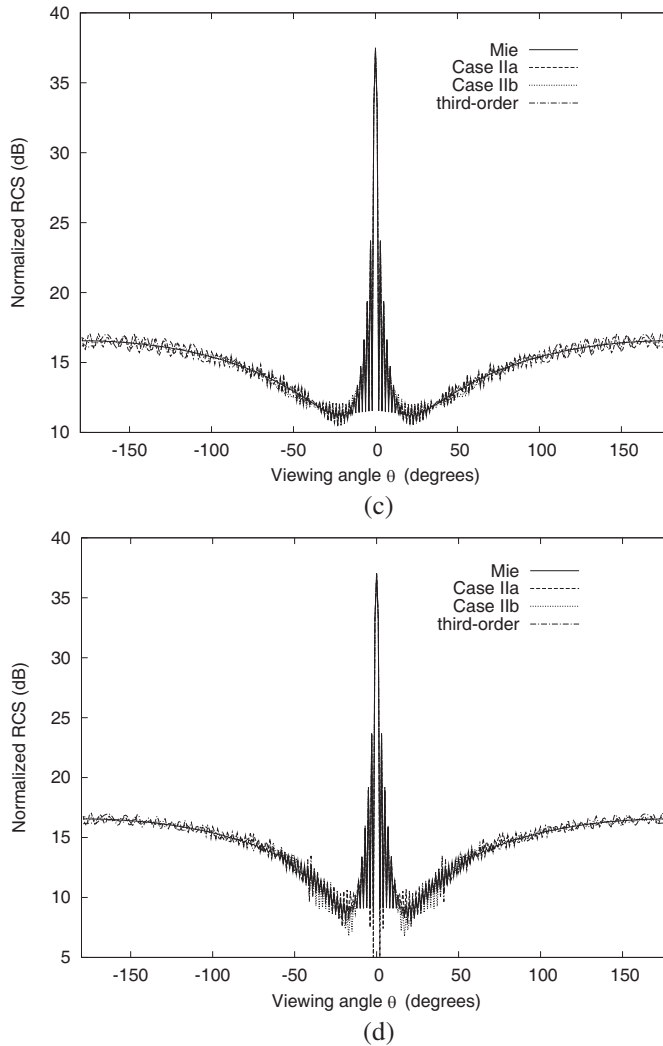


Figure 5. Case II implementation (first-order and coarse grid). (a) $a/\lambda = 9.6$, TM, (b) $a/\lambda = 9.6$, TE, (c) $a/\lambda = 14.4$, TM, (d) $a/\lambda = 14.4$, TE.

5. NUMERICAL SOLUTIONS — AIRFOIL

The proposed higher-order FVTD implementation is next used to compute scattering from a perfectly conducting NACA 0012 airfoil subject to broadside illumination. This is shown schematically in

Figure 6. The shadow boundary at the rounded leading edge of the airfoil ($\theta = \pm 180^\circ$) is similar to that encountered previously for the circular cylinder, while the sharp trailing edge ($\theta = 0^\circ$) can additionally constitute an edge discontinuity not present for a circular cylinder. Results are presented for TM and TE illumination for an electrical size corresponding to $a/\lambda = 10$, where a indicates the airfoil chord length. This problem was also solved by Shankar et al. [1] for TM illumination. As in [1], a body-fitted grid is employed. The grid topology is identical to that used previously for the circular cylinder, is shown in the form of a schematic in Figure 6. In the absence of an exact solution, results are validated against a “reference” solution obtained using a third-order ENO based FVTD scheme on an extremely fine grid consisting of 1600 grid points on the airfoil

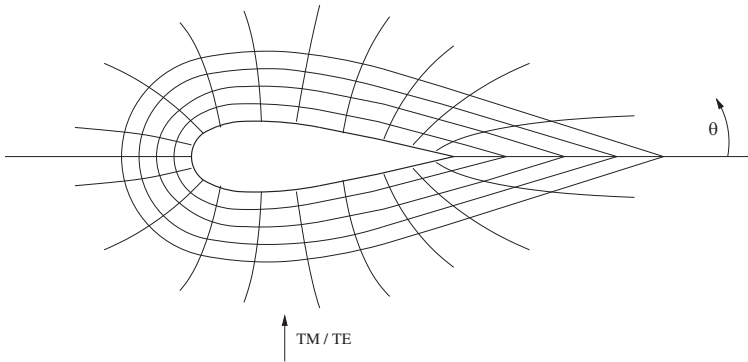


Figure 6. Airfoil — Illumination and grid, schematic.

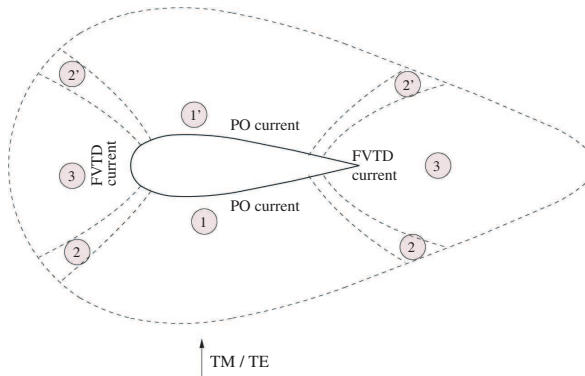


Figure 7. Airfoil — Case II implementation.

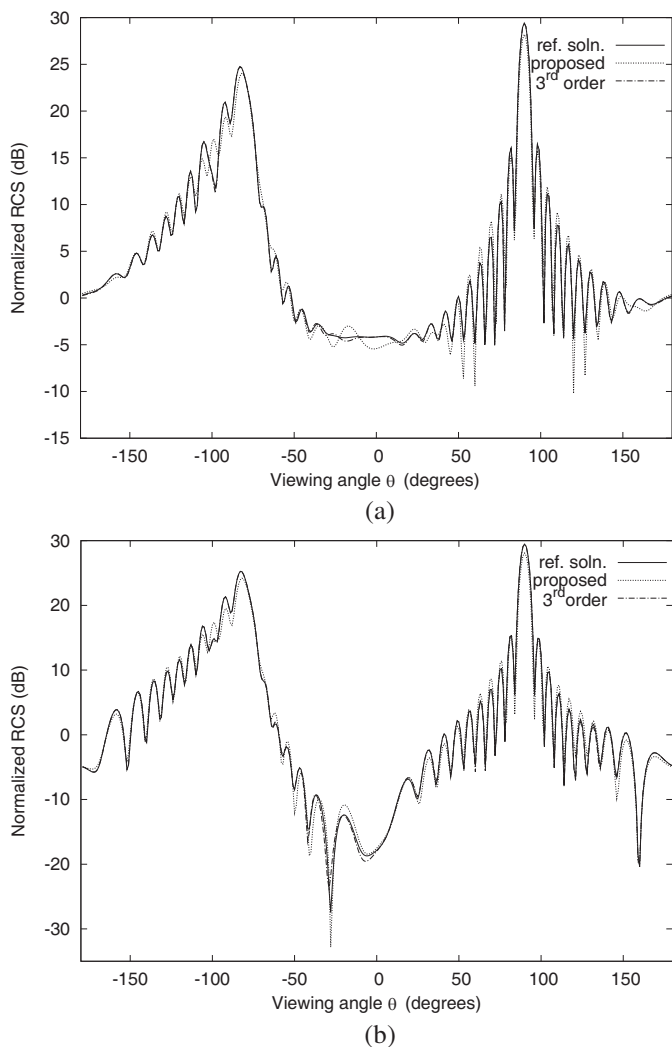


Figure 8. Scattering from a NACA 0012 airfoil. (a) $a/\lambda = 10$, TM, (b) $a/\lambda = 10$, TE.

surface which corresponds to a surface resolution of approximately 80 PPW. The number of grid points in the normal direction is fixed at 50. Case II implementation earlier described for the circular cylinder is considered for the airfoil. Higher-order FVTD computed surface currents are defined for the rounded leading edge and the sharp trailing edge as shown in Figure 7. As for a circular cylinder, region 3 involves

higher-order FVTD computations on a fine grid with an average surface resolution of approximately 15 PPW. Transition regions 2 and 2', which are few wavelengths long, connect FVTD parts to lit-PO and shadow-PO parts (see Figure 7). The FVTD method employs first-order spatial accuracy in PO regions (1 and 1'), where the average resolution on the bounding scatterer surface is only 3 PPW. Figures 8(a)–(b) compare bistatic RCS predicted using the proposed implementation with third-order ENO based FVTD results on an uniform fine grid and the reference solution. As in the case of a circular cylinder, results obtained using the proposed FVTD implementation with a PO approximated surface current valid for substantial parts of the scatterer, compares well with higher-order, fine-grid FVTD solutions.

6. CONCLUSION

The fine discretization required at high frequencies in terms of points-per-wavelength result in large simulation times, and seriously limits use of the FVTD method as an effective engineering tool. An efficient implementation of a higher-order FVTD scheme is proposed for computation of electromagnetic scattering from perfectly conducting scatterers with electrically large, smooth sections. Uniform higher-order and fine-grid accuracy are achieved in the computed results, despite using only first-order spatial accuracy and a coarse grid in substantial parts of the FVTD computational domain, by partially expressing the surface current using an asymptotic PO approximation. This can allow for a much faster FVTD analysis of geometries containing smooth, electrically large sections. This implementation, described here for two-dimensional geometries, should be readily extendable to three-dimensional FVTD or FDTD frameworks, and could be added as an utility in existing FVTD/FDTD codes for analyzing candidate geometries with electrically large, smooth parts.

ACKNOWLEDGMENT

This work was supported by Korea Research Foundation (KRF-2008-005-J01002) and the Flight Vehicle Research Center (UD070041AD).

REFERENCES

1. Shankar, V., W. F. Hall, and A. H. Mohammadian, "A time-domain differential solver for electromagnetic scattering problems," *Proceedings of the IEEE*, Vol. 77, No. 5, 709–721, May 1989.

2. Shankar, V., "A gigaflop performance algorithm for solving Maxwell's equations of electromagnetics," AIAA Paper 91-1578, June 1991.
3. Shang, J. S., "Characteristic-based algorithms for solving the Maxwell equations in the time domain," *IEEE Antennas and Propagation Magazine*, Vol. 37, No. 3, 15-25, 1995.
4. Yee, K. S. and J. S. Chen, "The finite-difference time domain (FDTD) and finite-volume time-domain (FVTD) methods in solving Maxwell's equations," *IEEE Transactions on Antennas and Propagation*, Vol. 45, No. 3, 354-363, 1997.
5. Chatterjee, A. and A. Shrial, "Essentially nonoscillatory finite volume scheme for electromagnetic scattering by thin dielectric coatings," *AIAA Journal*, Vol. 42, No. 2, 361-365, 2004.
6. Bhattacharya, A. and A. Chatterjee, "Finite volume time-domain computations for electromagnetic scattering from intake configurations," *Journal of Aircraft*, Vol. 42, No. 2, 572-573, 2005.
7. Georgakopoulos, S. V., C. R. Britcher, C. A. Balanis, and R. A. Renaut, "Higher-order finite-difference schemes for electromagnetic radiation, scattering, and penetration, Part I: Theory," *IEEE Antennas and Propagation Magazine*, Vol. 44, No. 1, 134-142, 2002.
8. Wang, S. and F. L. Teixeira, "Grid-dispersion error reduction for broadband FDTD electromagnetic simulations," *IEEE Transactions on Magnetics*, Vol. 40, No. 2, 1440-1443, 2004.
9. Okoniewski, M., E. Okoniewska, and M. A. Stuchly, "Three-dimensional subgridding algorithm for FDTD," *IEEE Transactions on Antennas and Propagation*, Vol. 45, No. 3, 422-428, 1997.
10. Djordjevic, M. and B. M. Notaros, "Higher order hybrid method of moments-physical optics modeling technique for radiation and scattering from large perfectly conducting surfaces," *IEEE Transactions on Antennas and Propagation*, Vol. 53, No. 2, 800-813, 2005.
11. Abdel Moneum, M. A., X. Shen, J. L. Volakis, and O. Graham, "Hybrid PO-MOM analysis of large axi-symmetric radomes," *IEEE Transactions on Antennas and Propagation*, Vol. 49, No. 12, 1657-1666, 2001.
12. Yangi, L.-X., D.-B. Ge, and B. Wei, "FDTD/TDPO hybrid approach for analysis of the EM scattering of combinative objects," *Progress In Electromagnetics Research*, PIER 76, 275-284, 2007.
13. Chou, H.-T. and H.-T. Hsu, "Hybridization of simulation codes

- based on numerical high and low frequency techniques for the efficient antenna design in the presence of electrically large and complex structures,” *Progress In Electromagnetics Research*, PIER 78, 173–187, 2008.
14. Fumeaux, C., D. Baumann, P. Leuchtman, and R. Vahldieck, “A generalized local time-step scheme for efficient FVTD simulations in strongly inhomogeneous media,” *IEEE Transactions on Microwave Theory and Techniques*, Vol. 52, No. 3, 1067–1076, 2004.
 15. Firsov, D. K. and J. LoVetri, “FVTD-integral equation hybrid for Maxwell’s equations,” *International Journal of Numerical Modelling: Electronic Networks, Devices and Fields*, Vol. 21, 29–42, 2007.
 16. Burkholder, R. J. and T.-H. Lee, “Adaptive sampling for fast physical optics numerical integration,” *IEEE Transactions on Antennas and Propagation*, Vol. 53, No. 5, 1843–1845, 2005.
 17. Chatterjee, A. and R.-S. Myong, “Modified finite volume time domain method for efficient prediction of radar cross section at high frequencies,” *Journal of the Korea Institute of Electromagnetic Engineering and Science*, Vol. 8, No. 3, 100–109, 2008.
 18. Shu, C. W. and S. Osher, “Efficient implementation of essentially non-oscillatory shock-capturing schemes,” *Journal of Computational Physics*, Vol. 77, No. 2, 439–471, 1988.
 19. Shu, C. W. and S. Osher, “Efficient implementation of essentially non-oscillatory shock-capturing schemes II,” *Journal of Computational Physics*, Vol. 83, No. 1, 32–78, 1989.
 20. LeVeque, R. J., *Numerical Methods for Conservation Laws*, Birkhauser Verlag, 1992.
 21. Gupta, I. J. and W. D. Burnside, “A physical optics correction for backscattering from curved surfaces,” *IEEE Transactions on Antennas and Propagation*, Vol. 35, No. 5, 553–561, 1987.
 22. Balanis, C. A., *Advanced Engineering Electromagnetics*, John Wiley and Sons, Inc., 1989.